NANO LETTERS

pubs.acs.org/NanoLett
Letter

Interplay of Landau Quantization and Interminivalley Scatterings in a Weakly Coupled Moiré Superlattice

Yalong Yuan,[#] Le Liu,[#] Jundong Zhu, Jingwei Dong, Yanbang Chu, Fanfan Wu, Luojun Du, Kenji Watanabe, Takashi Taniguchi, Dongxia Shi, Guangyu Zhang,* and Wei Yang*

Cite This: *Nano Lett.* 2024, 24, 6722−6729

Read Online

ACCESS | Metrics & More | Article Recommendations | Supporting Information

ABSTRACT: Double-layer quantum systems are promising platforms for realizing novel quantum phases. Here, we report a study of quantum oscillations (QOs) in a weakly coupled double-layer system composed of a large-angle twisted-double-bilayer graphene (TDBG). We quantify the interlayer coupling strength by measuring the interlayer capacitance from the QOs pattern at low temperatures, revealing electron−hole asymmetry. At high temperatures when SdHOs are thermally smeared, we observe resistance peaks when Landau levels (LLs) from two moiré minivalleys are aligned, regardless of carrier density; eventually, it results in a 2-fold increase of oscillating frequency in D, serving as compelling evidence of the magneto-intersub-band oscillations (MISOs) in double-layer systems. The temperature dependence of MISOs suggests that electron−electron interactions play a crucial role and the scattering times obtained from MISO thermal damping are correlated with the interlayer coupling strength. Our study reveals intriguing interplays among Landau quantization, moiré band structure, and scatterings.

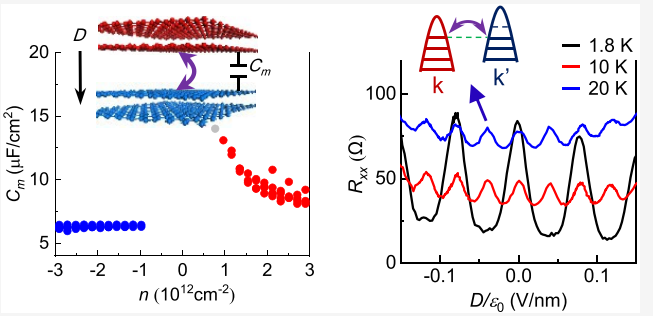

KEYWORDS: *double-layer quantum system, magneto-intersub-band oscillations, interminivalley scatterings, interlayer capacitance, twisted-double-bilayer graphene*

Double-layer quantum systems are ideal platforms for realizing novel quantum phases,[1−9] thanks to the rich interplay among charge, spin, and layer degree of freedom. Recently, twisted-graphene multilayers have been demonstrated as a promising paradigm for developing novel states of matter.[10−18] A key ingredient lies in the twist angle, which determines not only the lateral size of the moiré superlattice in real space, i.e., moiré Brillouin zone in reciprocal space, but also the coupling between the layers. At some optimal angle, strong interlayer coupling will lead to flat moiré bands with the hybridized electronic states indistinguishable between the two layers, which favors correlated states.[19−23] At a larger angle, in the so-called weak coupling regime, the moiré superlattice reduces in size and the moiré bands are usually dispersive with a reduced Fermi velocity, and importantly the wave function of the minivalley is layer polarized.[24−28] Essentially, the interlayer coupling defines the electronic correlation between two layers, and tuning this coupling is crucial for realizing the collective quantum phases in various double-layer systems. The ability to quantify the coupling in double-layer systems is important, yet rarely explored.

Here, we focus on a weakly coupled double-layer moiré system, which is composed of a large-angle twisted-double-bilayer graphene (TDBG), by measuring the quantum oscillations (QOs) due to Landau quantization. The QOs, in principle, are determined by the combined band structure of the two layers and thus could serve as a probe for interlayer coupling. The displacement field (D) is a powerful knob in tuning electronic structure in TDBG. In the strong coupling regime, it helps to reveal spin-polarized correlated insulators and valley-polarized insulators at different D,[12−14,29−31] and it even leads to anomalous QOs in insulators where field-induced sub-band hybridizations are important.[32] In the weak coupling regime, D drives a charge redistribution between the two layers, or equivalently between two minivalleys.[24,26,27] The interlayer scatterings are equivalent to the interminivalley scatterings, as shown in Figure 1b,e. For a twist angle of around 2°, due to the small size of the moiré Brillion zone (Figure 1c), scatterings between minivalleys could be significant.[25,27] Inspired by the pioneering works of minivalley scatterings in TBG[25] and TDBG,[27] we target the unexplored issue of the interplay between interlayer coupling and interminivalley scatterings by measuring the QOs in high-quality TDBG

Received: March 25, 2024
Revised: May 2, 2024
Accepted: May 2, 2024
Published: May 8, 2024

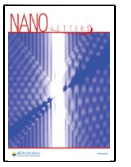

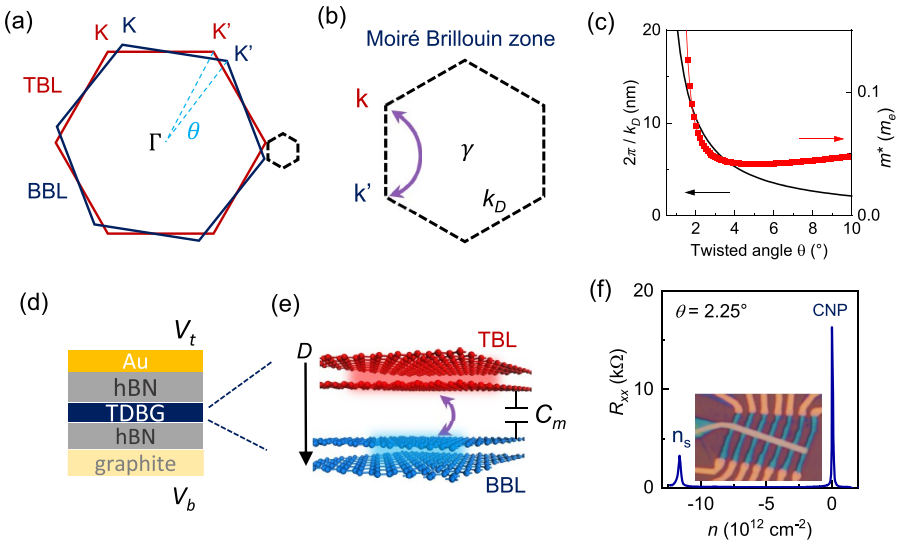

Figure 1. A weakly coupled moiré system of twisted double bilayer graphene (TDBG). (a) The two Brillouin zones of the top bilayer (TBL, red) and bottom bilayer (BBL, blue), with a twist angle (θ). (b) The moiré Brillouin zone, with the moiré valleys k (red) and k' (blue) from the top and bottom layers, respectively. k_D is the momentum difference between k and k' valley in the moiré Brillouin zone, and $2\pi/k_D$ corresponds to the length scale of interminivalley scattering. The curved arrow (purple) denotes the intervalley scatterings. (c) $2\pi/k_D$ (black) and the effective mass (red) as a function of twist angle from band structure calculations in TDBG. (d) Side-view schematic of the stacked TDBG device structure. (e) Schematic of the interlayer capacitance (C_m) between the top bilayer (TBL) and bottom bilayer (BBL) in TDBG, with the curved arrow (purple) indicating the interlayer scatterings. (f) A typical transfer curve of $R_{xx}(n)$ at T = 1.8 K for device D1 and a twist angle of ∼2.25° obtained from carrier density at full fillings of the moiré superlattice (n_s). The inset shows the Hall bar structure of D1.

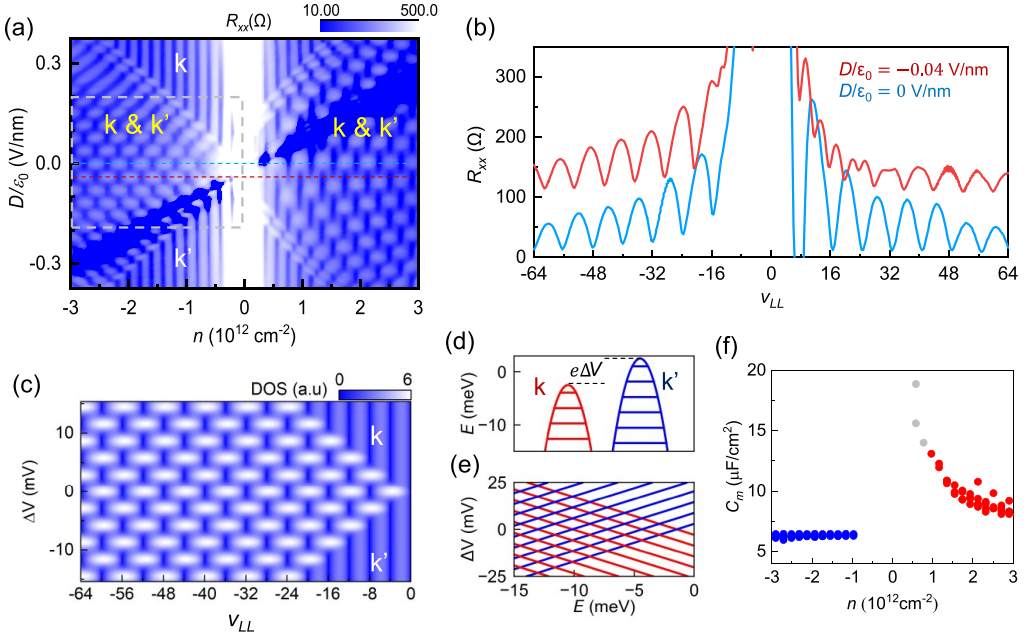

Figure 2. Quantifying the interlayer coupling strength from the quantum oscillation spectra in a capacitance model. (a) Color mapping of $R_{xx}(\nu_{LL}, D/\varepsilon_0)$ at T = 1.8 K and B = 2 T. (b) Plots of R_{xx} at D/ε_0 = 0 and −0.04 V/nm, corresponding to the blue and red dotted lines in (d), respectively. The red line is offset by 100 Ω for clarity. (c) Calculated DOS as a function of Landau level (LL) filling factor ν_{LL} and interlayer potential difference ΔV at B = 2 T. (d) Schematic of the parabolic approximation for the minivalley k (red) and k' (blue) and the LL structure in magnetic field for DOS calculation. (e) Evolution of the LL spectra of k and k' as a function of energy E and the interlayer potential difference ΔV at B = 2 T. (f) The measured C_m versus n, where C_m is extracted from the intersection pattern in (a) according to the capacitance model. C_m at a small electron density of $<10^{12}$/cm^2 is marked in gray.

devices. In the following, we will first quantify the interlayer coupling strength from the periodicity of the QOs at low temperatures in a capacitance model of D-field tuned Shubnikov-de Haas oscillations (SdHOs) from two minivalleys, yielding electron−hole asymmetry. Then, we reveal a 2-fold increase of oscillating frequency in D for the QOs at elevated temperatures when SdHOs are thermally smeared, and we attribute them to the enhanced interminivalley scatterings when the Landau levels (LLs) at k and k' minivalleys are aligned. Lastly, we demonstrate an intimate connection between interlayer coupling strength and the

https://doi.org/10.1021/acs.nanolett.4c01411
Nano Lett. 2024, 24, 6722−6729

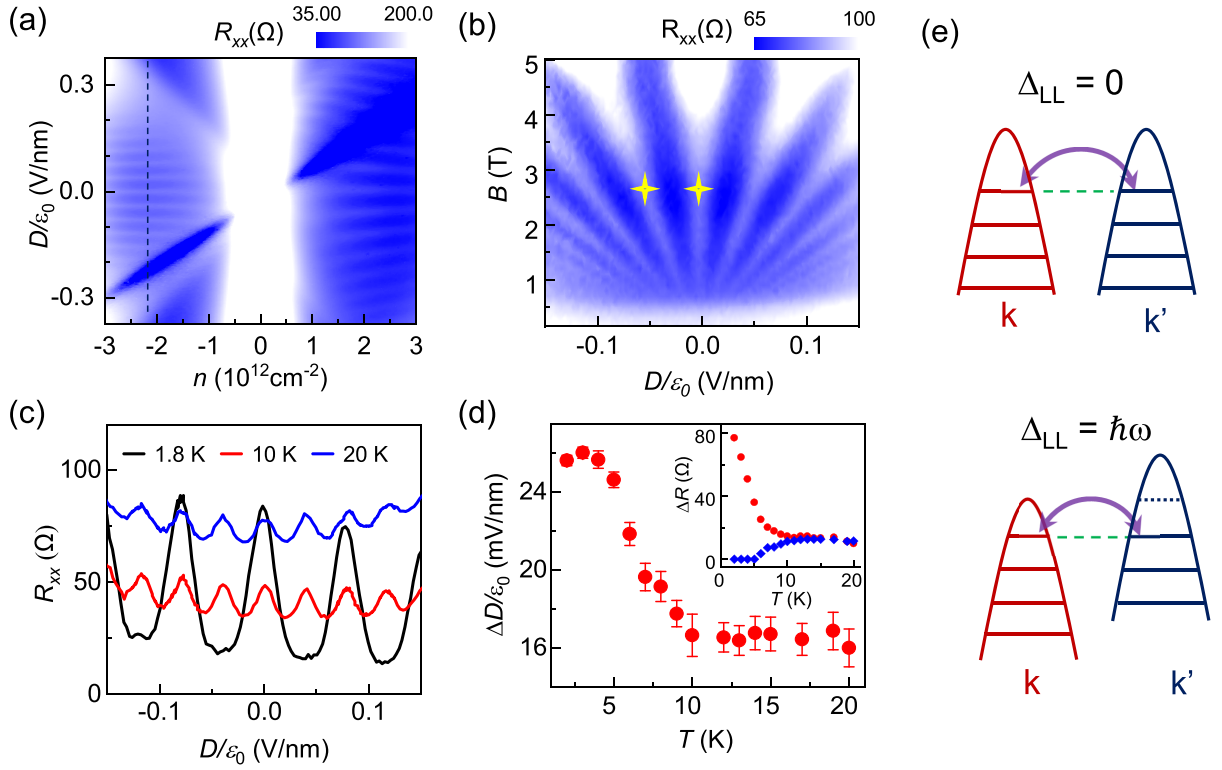

Figure 3. Displacement field dependence of the carrier density insensitive quantum oscillations. (a) R_{xx} as a function of n and D/ε_0 at B = 2 T and T = 20 K. (b) R_{xx} as a function of D/ε_0 and B at $n = -2.18 \times 10^{12}$/cm^2 and T = 20 K. (c) R_{xx} versus D/ε_0 at T = 1.8, 10, and 20 K. Here B = 2 T and $n = -2.18 \times 10^{12}$/cm^2 corresponding to the blue dotted line in (a). (d) $\Delta D/\varepsilon_0$ versus T, where $\Delta D/\varepsilon_0$ is the fwhm of the resistance peak at $D/\varepsilon_0 = 0$ in (c). Inset: amplitude of resistance peaks ΔR_{xx} versus T at $D/\varepsilon_0 = 0$ (red) and $D/\varepsilon_0 = 0.043$ V/nm (blue). (e). Schematics of the enhanced intervalley scatterings at the resonant condition when LLs from k and k' are aligned, corresponding to the yellow stars in (b). The green dashed lines denote the Fermi level.

interminivalley scatterings by quantifying the scattering lifetime from the high-temperature oscillating magnetoresistance.

We fabricate ultraclean TDBG devices by cut and stack methods.[33−35] In the following, we focus on device D1 with a twist angle of 2.25° that reveals high-quality oscillation data with a low resistance of a few tens of ohms. The device is in a dual-gate geometry, allowing an independent tuning of total carrier density n and displacement field D, i.e. $n = (C_tV_t + C_bV_b)/e$ and $D/\varepsilon_0 = (C_tV_t - C_bV_b)/2/\varepsilon_0$, where C_b (C_t) is the geometrical capacitance per area for the bottom (top) gate, e is the electron charge, and ε_0 is the vacuum permittivity. Figure 2a is a color mapping of measured longitudinal resistance R_{xx} as a function of n and D/ε_0 at B = 2 T. The oscillations due to Landau quantization are vividly revealed in the alternating changes of the color between blue and white, resulting in a grid pattern from the combined effects of Landau quantization and displacement field D. The oscillation data are plotted in Figure 2b, where the resistance is minimum at LL filling factor $\nu_{LL} = 8N$ for $D/\varepsilon_0 = 0$ and at $\nu_{LL} = 8(N + 1/2)$ for $D/\varepsilon_0 = -0.04$ V/nm, with N being a nonzero integer. The data are of high quality, with a resistance minimum of ∼15 Ω and oscillation amplitude of ∼60 Ω at around $\nu_{LL} = -50$. Here, $\nu_{LL} = n\Phi_0/B$ is the LL filling factor and Φ_0 is the magnetic flux quantum.

To begin with, we consider Landau level crossings of the two minivalleys that are approximated as two layer-polarized parabolic energy bands (Figure 2d). They are quantized into a series of Landau levels (LLs) at a given B, described by

$$E_{t/b} = \alpha(|N_{t/b}| + 1/2)\hbar\omega \mp e\Delta V/2 \quad (1)$$

Here t/b corresponds to the top/bottom layer, $\alpha = +1$ (-1) for electron (hole), N is the Landau level index, $\hbar$ is the reduced Planck constant, $\omega = eB/m^*$ is the cyclotron frequency, and ΔV is the interlayer potential difference that depends on D. With the change of ΔV, the two sets of LLs will intersect each other as shown in Figure 2e. As shown in Figure 1c, the effective mass m^* in TDBG is twist angle dependent and is usually larger than that in bilayer graphene.[36,37] By taking $m^* = 0.08\ m_e$ and an LL broadening of 0.35 $\hbar\omega$, the calculated Landau level DOS mapping for the holes (see details in Methods) is shown in Figure 2c. The calculations agree well with the experimental data, as shown by the comparison in Supplementary Figure S6. For fixed total LL filling factors, both the calculated and experimental data show periodic intersection arrays, and their resemblance indicates a close relationship between ΔV and D in the moiré valence band.

Next, we quantitatively analyzed the QOs to reveal the intimate link between ΔV and D. The TDBG device follows a capacitive model[38−40] (Figure 1e and details in Supplementary Note 3), and it gives

$$\Delta V = (\Delta - e\Delta n/2)/C_m \quad (2)$$

where C_m is the measured interlayer capacitance and Δn is the carrier density difference between the top and bottom bilayer graphene. The magnitude of interlayer capacitance C_m reflects the degree of layer polarization,[41,42] and the larger the C_m the stronger the coupling between two twisted layers. Experimentally, we can extract the interlayer capacitance C_m according to eq 2. At the intersection point of two sets of

https://doi.org/10.1021/acs.nanolett.4c01411
Nano Lett. 2024, 24, 6722−6729

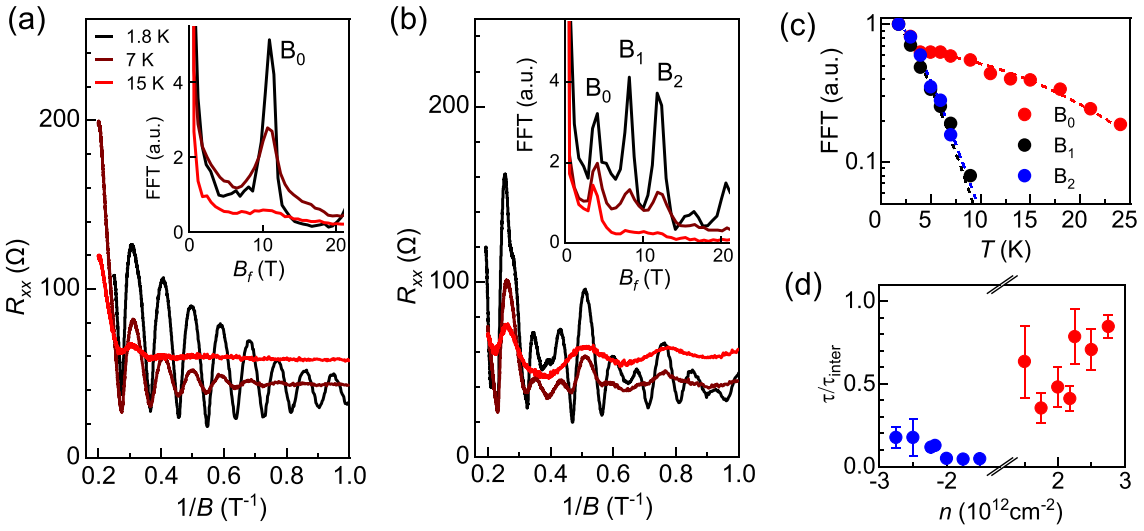

Figure 4. Temperature dependence of the quantum oscillations. (a, b) Temperature-dependent $R_{xx}(1/B)$ for D/ε_0 = 0 and −0.08 V/nm, respectively, where n is fixed at $-2.16 \times 10^{12}/\mathrm{cm}^2$. The insets are FFT spectra. (c) Normalized FFT amplitude verse T for the modes B_0, B_1, and B_2 in (b). The B_0 mode is fitted with $\exp(-\gamma T^2)$ decay, while B_1 and B_2 are fitted with the L-K formula. (d) The ratio $\tau/\tau_{\mathrm{inter}}$ versus n at T = 18 K, where $\tau/\tau_{\mathrm{inter}}$ is extracted by fitting the high-temperature magnetoresistance curve with the eq 3.

LLs in Figure 2a,c, one could obtain $\Delta n = (N_t - N_b) \times 4eB/h$ and $\Delta V = (N_t - N_b) \times \hbar B/m^*$, where m^* is 0.073 m_e for holes and 0.06 m_e for electrons extracted from the thermal damping effect of QOs at D/ε_0 = 0 (see Supplementary Figure S10). The obtained C_m is plotted against n in Figure 2f. For the valence band, $C_m \approx 6.3\ \mu\mathrm{F/cm}^2$ is constant, regardless of n; this suggests the valence band is a well-defined weakly coupled system.[38,42] For the conduction band, on the contrary, it shows a strong carrier density dependence. C_m reaches up to ∼13 μF/cm^2 at a low density of around $1 \times 10^{12}/\mathrm{cm}^2$, and it decreases and tends to saturate at a small value of ∼8 μF/cm^2 at a high density of around $3 \times 10^{12}/\mathrm{cm}^2$ as shown in Figure 2c. Such a large capacitance indicates a strong coupling in the conduction band, and its strong doping dependence suggests that the interlayer coupling strength is highly sensitive to the change of the Fermi surface. Note that similar results are reproduced in device D2 (Supplementary Figure S16). It is also worth noting that the observed electron−hole asymmetry in the capacitance model matches well with our continuum model calculations, where the degree of layer polarization for holes is higher than that for electrons (Supplementary Figure S4).

To investigate the interlayer scattering processes in the weakly coupled double-layer system, we measured the QOs at high temperatures. Figure 3a shows a color mapping of longitudinal resistance $R_{xx}(n, D/\varepsilon_0)$ at B = 2 T and T = 20 K, and it reveals a striped pattern, unlike the previous grid pattern at low temperature. The disappearance of oscillating $R_{xx}(n)$ at a fixed D indicates that conventional SdHOs are thermally smeared. The striped patterns depend only on D, irrespective of total carrier density n; in other words, the strip patterns are determined only by the carrier density difference between the top and bottom layers (k and k' minivalley). The observation agrees perfectly with the resonant condition when LLs from two minivalleys are aligned and are the main features of the magneto-intersub-band oscillations (MISOs).[43−49] Note that similar striped patterns are observed in ref 27; by comparison, we could investigate MISO physics in more detail, thanks to the high-quality data in our device. Take the dashed line in Figure 3a for example; comparisons of $R_{xx}(D/\varepsilon_0)$ at different T are shown in Figure 3c. For the first time, the transition from SdHO to MISO is captured in the doubling of D periodicity as T is increased from 1.8 to ≥10 K. Such transition is also vividly captured in the temperature evolution of the peak width and peak amplitude at D/ε_0 = 0 in Figure 3d; it decreases rapidly from ∼26 mV/nm at T < 4 K to ∼16 mV/nm at 10 K, and then it barely changes at $T \geq$ 10 K. Note that, by considering the spacing between peaks at $T \geq$ 10 K as $\hbar\omega$, a peak width of ∼16 mV/nm corresponds to an energy line width of ∼1.85 meV. In addition, the high-temperature MISOs are found emanating from D/ε_0 = 0 at B = 0 T in Figure 3b, which resembles the conventional Landau fan diagram when n is varied. The resemblance indicates that the carrier density difference between the two minivalleys is linearly generated by D. And most importantly, the resistance peak at D/ε_0 = 0 indicates additional scattering processes for the resonant condition, as shown in the schematics of Figure 3e, which is exactly the predicted interminivalley scatterings in the MISO model. Similar observations are obtained for electrons in Supplementary Figures S8 and S9.

To further establish a close connection between the interlayer coupling obtained at low temperature and the interminivalley scatterings at high temperature, we measured the resistance as a function of B at high temperature. At a fixed carrier density of $-2.16 \times 10^{12}/\mathrm{cm}^2$ in the valence band, the temperature (T)-dependent QOs are plotted against $1/B$ for D/ε_0 = 0 and −0.08 V/nm in Figure 4a,b, respectively. For D/ε_0 = −0.08 V/nm, it evolves from a beating pattern at low T to a single frequency oscillation at high T. The changes are better revealed in the fast Fourier transform (FFT) spectrum in the inset of Figure 4b, where the oscillation frequency (B_f) changes from three peaks at T = 1.8 K to one peak at T = 15 K. By contrast, for D/ε_0 = 0 V/nm in Figure 4a, $B_f \approx$ 11 T remains unchanged while its amplitude quickly fades, as T is increased. Note that frequency B_f is linearly correlated with n, defined as $B_f = nh/ge$. Considering the degeneracy g = 4 for each minivalley, the total degeneracy is 8 at D/ε_0 = 0 V/nm and $B_f \approx$ 11 T corresponds to $n = 2.13 \times 10^{12}/\mathrm{cm}^2$ that matches well with the gate-induced carrier density, which is then assigned as SdHO. At nonzero D/ε_0 = −0.08 V/nm, the minivalley degeneracy is lifted, and the three oscillation modes at $B_f \approx$ 4,

https://doi.org/10.1021/acs.nanolett.4c01411
Nano Lett. 2024, 24, 6722−6729

8.2, and 12.2 T in Figure 4b correspond to n = 0.387, 0.794, and 1.181 × 10^{12}/cm^2, respectively. The two high-frequency modes in Figure 4b share the same T dependence as the one in Figure 4a and are attributed to the SdHO in two minivalley k and k'. What's more, the lowest frequency mode at B_f = 4 T is equal to the difference $B_f(k) - B_f(k')$; in other words, the slow oscillation mode is determined by the carrier density difference Δn between k and k' minivalleys. The low-frequency mode that could persist at high T resembles the high-temperature QOs in weakly coupled TBG in ref 25, which is another characteristic of MISO[43−48] in TDBG.

The details of the scattering lifetime are quantitatively revealed in the thermal damping of the QOs. The thermal damping of SdHO is described by the Lifshitz−Kosevich (L-K) formula, i.e., $R(T) \approx (2\pi^2 k_B T/\hbar\omega)/\sinh(2\pi^2 k_B T/\hbar\omega)$. As shown in Figure 4c, the amplitude of SdHO is barely visible at T = 10 K, and similar T dependence for B_1 and B_2 indicates identical effective mass for the minivalleys. By contrast, MISOs observed in Figure 4c are thermally damped with a slow temperature dependence described as $\exp(-\gamma T^2)$ (Figure 4c). In a clean limit ($\omega\tau \gg 1$, τ is the total scattering time)[43,44,46,50,51] with the assumption of identical scattering time for two minivalley, MISO in TDBG could be described as

$$\Delta\rho = 2(\tau/\tau_{inter})\rho_0 \exp(-2\pi/(\omega\tau_q)) \cos(2\pi(E_t - E_b)/\hbar\omega) \quad (3)$$

Here ρ_0 is the Drude resistivity, τ and τ_{inter} are the total and interminivalley scattering times, respectively, and $\exp(-2\pi/(\omega\tau_q))$ is the Dingle factor, with τ_q being the quantum scattering time. The observed decay of $\exp(-\gamma T^2)$ indicates a scattering rate of $\sim T^2$, which further suggests an important role played by electron−electron interaction.[46] It is worth mentioning that the low resistance, tens of ohms in device D1, as well as repeatable results in device D2, enables us to reveal the intrinsic MISO and to rule out other extrinsic impurities or phonon scattering mechanisms, distinct from the previous report on TDBG. We attribute the prominent quadratic law to the enhanced Umklapp electron scatterings in the moiré system, which also agrees with the quadratic power law of zero-field resistivity at low temperatures shown in Supplementary Figure S14 when phonon contributions are negligible in TDBG.[52,53] At a fixed T = 18 K, $\log(\Delta\rho)$ vs $1/B$ gives the quantum scattering time $\tau_q \approx$ 1.04 ps, which is of the same order of magnitude compared to the mean free time; by changing T, we could obtain τ_q vs T (see Supplementary Figure S12). In addition, we can quantitively extract the ratio τ/τ_{inter} by fitting the high-temperature magnetoresistance curve with eq 3. Figure 4d shows the obtained τ/τ_{inter} values for both the electrons and holes. For holes, the ratio is small, ranging from 0.048 to 0.2, indicating a small intervalley scattering rate $\Gamma \approx 1/\tau_{inter}$, while for electrons it is much larger, ranging from ∼0.4 to 0.8, indicating a comparable contribution between intravalley and intervalley scatterings. For instance, at a fixed n = ±2.0 × 10^{12}/cm^2 and T = 18 K (Supplementary Figures S11 and S13), one could obtain intervalley scatter times of ∼120 and ∼6 ps for holes and electrons, respectively. It is worth noting that the obtained τ/τ_{inter} also agrees well with the electron−hole asymmetric interlayer coupling from C_m in Figure 2c, thus establishing an intimate connection between intervalley scatterings and interlayer couplings.

In conclusion, we systematically investigate the interlayer coupling and interminivalley scatterings from quantum oscillations in a weakly coupled moiré superlattice of TDBG. The low-temperature QOs reveal that the valence band is a well-defined weakly coupled system, whereas the interlayer coupling strength of the conduction band highly depends on the doping levels, indicating strong electron−hole asymmetry. In addition, high-temperature QOs demonstrate strong interminivalley scattering in this system according to the observed MISO for both electrons and holes when LLs from the two minivalleys are aligned. The MISO can be effectively tuned by D, via $\Delta E(D) \approx D$; the temperature dependence of MISO suggests electron−electron interactions and interlayer couplings play a crucial role in the interlayer scatterings. Being a highly tunable moiré system, TDBG provides an excellent platform to investigate the interplay among Landau quantization, moiré band structure, and scatterings.

METHODS

Device Fabrication and Characterization. The twisted-double-bilayer graphene (TDBG) devices are fabricated by the cut and stack technique.[33] Bilayer graphene, few-layer graphite (FLG), and hexagonal boron nitride (h-BN) (15−40 nm thick) were first exfoliated on the SiO_2 substrate. As shown in Supplementary Figure S1, the layer number of graphene is identified by the reflection contrast from the optical microscope images[54] as well as the Raman spectrum.[55] Then we used an atomic force microscope (AFM) needle to cut a large bilayer graphene flake into two pieces. Next, we used poly(bisphenol A carbonate) (PC) supported by polydimethylsiloxane (PDMS) on a glass slide to pick up the top h-BN, two pieces of bilayer graphite with a twist angle of 60° + θ, bottom h-BN, and a bottom graphite gate in turn.

The fabrication of the metal top gate and electrodes followed a standard electron-beam lithography process and electron-beam metal evaporation. The devices were designed as a Hall bar structure and shaped by traditional reactive ion etching with a CHF_3 and O_2 gas mixture. Finally, Cr/Au electrodes were evaporated on a silicon wafer as 1D edge contacts to connect with Hall bars. The combination of two gate voltages allows independent tuning of the carrier density n and D, i.e. $n = (C_tV_t + C_bV_b)/e$ and $D = (C_tV_t - C_bV_b)/2$.

The transport behaviors are measured at the base temperature (∼1.8 K) of our helium-4 cryostat. As shown in Supplementary Figure S2, the twist angle of the TDBG devices is determined by the carrier density difference between CNP and gap opening at full filling, i.e. $n_s = 4/A \approx 8\theta/(\sqrt{3}a^2)$, where A is the area of a moiré unit cell, θ is the twist angle, and a is the lattice constant of graphene.

Continuum Model Calculations. The band structure of TDBG was calculated by a continuum model.[19,56] In the calculation, we use the parameters from refs 27 and 56

$$(\gamma_0, \gamma_1, \gamma_3, \gamma_4, w_{AA}, w_{AB}) = (3100, 400, 320, 44, 100, 100)\ \text{meV}$$

Here γ_0 is the intralayer nearest-neighbor hopping term, γ_1 is the interlayer hopping term in AB-stacked bilayer graphene, from bottom layer A sublattice to top layer B sublattice, γ_3 is the interlayer hopping term from bottom layer B sublattice to top layer A sublattice, and γ_4 is the interlayer hopping term from bottom layer A(B) sublattice to top layer A(B) sublattice. γ_3 and γ_4 will bring electron−hole asymmetry in twisted-double-bilayer graphene systems. The electric displacement

https://doi.org/10.1021/acs.nanolett.4c01411
Nano Lett. 2024, 24, 6722−6729

field changes the on-site energy of every layer in twisted graphene systems, described by the matrix

$$V = \begin{pmatrix} \frac{U}{2}\hat{1} & 0 & 0 & 0 \\ 0 & \frac{U}{6}\hat{1} & 0 & 0 \\ 0 & 0 & -\frac{U}{6}\hat{1} & 0 \\ 0 & 0 & 0 & -\frac{U}{2}\hat{1} \end{pmatrix}$$

where U is the electrostatic interlayer potential energy and $\hat{1}$ is a 2×2 unit matrix.

Landau Level Spectrum Calculations. The band structures of k and k' minivalleys are approximately equivalent to two parabolic bands localized in the top and bottom layers, respectively. Now we focus on the case of hole-type valence band. The Landau level energy spectrum can be described by the formulas

$$E_{tN} = -(|N| + 1/2)\hbar\omega - eV_0/2$$

$$E_{bN} = -(|N| + 1/2)\hbar\omega + eV_0/2$$

$$\omega = eB/m^*$$

Next, we calculate the density of states (DOS) of Landau levels based on the Gauss distribution by considering the disorder induced Landau level broadening

$$D_N(E) = gn_L\sqrt{\frac{2}{\pi\Gamma^2}}\exp\left(-2\frac{(E - E_N)^2}{\Gamma^2}\right)$$

Here, Γ corresponds to the broaden of Landau levels, and we use an estimation of $\Gamma/\hbar w = 0.35$ to fit our experimental data. g is the degeneracy of the energy band, and n_L is the carrier density to fully fill a Landau level. At a fixed interlayer voltage ΔV, DOS can be expressed as

$$D(E) = \sum_N (D_N^{up}(E) + D_N^{down}(E))$$

The filling factor ν is calculated by integrating DOS with E

$$\nu = \frac{n}{n_L} = \frac{1}{n_L}\int D(E)\,dE$$

ASSOCIATED CONTENT

Supporting Information

The Supporting Information is available free of charge at https://pubs.acs.org/doi/10.1021/acs.nanolett.4c01411.

Identification of the thickness of graphene flakes, characterizations and the twist angle extraction in TDBG device D1, continuum model calculations, electrostatic equation and capacitance model, comparison between the theoretical simulation and experimental result, the influence of a dc electric current I_{dc} in D1, MISO in the conduction band in D1, additional measurements of QOs at $B = 2$ T in D1, effective mass of electrons and holes in D1, scattering time and Fermi liquid behaviors in TDBG in D1, D tunable Landau fan diagram at $T = 1.8$ K in D1, and repeatable results in TDBG device D2 (PDF)

AUTHOR INFORMATION

Corresponding Authors

Guangyu Zhang − *Beijing National Laboratory for Condensed Matter Physics and Institute of Physics, Chinese Academy of Sciences, Beijing 100190, People's Republic of China; School of Physical Sciences, University of Chinese Academy of Sciences, Beijing 100190, People's Republic of China; Songshan Lake Materials Laboratory, Dongguan 523808, People's Republic of China*; Email: gyzhang@iphy.ac.cn

Wei Yang − *Beijing National Laboratory for Condensed Matter Physics and Institute of Physics, Chinese Academy of Sciences, Beijing 100190, People's Republic of China; School of Physical Sciences, University of Chinese Academy of Sciences, Beijing 100190, People's Republic of China; Songshan Lake Materials Laboratory, Dongguan 523808, People's Republic of China*; orcid.org/0000-0002-3925-0352; Email: wei.yang@iphy.ac.cn

Authors

Yalong Yuan − *Beijing National Laboratory for Condensed Matter Physics and Institute of Physics, Chinese Academy of Sciences, Beijing 100190, People's Republic of China; School of Physical Sciences, University of Chinese Academy of Sciences, Beijing 100190, People's Republic of China*

Le Liu − *Beijing National Laboratory for Condensed Matter Physics and Institute of Physics, Chinese Academy of Sciences, Beijing 100190, People's Republic of China; School of Physical Sciences, University of Chinese Academy of Sciences, Beijing 100190, People's Republic of China*

Jundong Zhu − *Beijing National Laboratory for Condensed Matter Physics and Institute of Physics, Chinese Academy of Sciences, Beijing 100190, People's Republic of China; School of Physical Sciences, University of Chinese Academy of Sciences, Beijing 100190, People's Republic of China*

Jingwei Dong − *Beijing National Laboratory for Condensed Matter Physics and Institute of Physics, Chinese Academy of Sciences, Beijing 100190, People's Republic of China; School of Physical Sciences, University of Chinese Academy of Sciences, Beijing 100190, People's Republic of China*

Yanbang Chu − *Beijing National Laboratory for Condensed Matter Physics and Institute of Physics, Chinese Academy of Sciences, Beijing 100190, People's Republic of China; School of Physical Sciences, University of Chinese Academy of Sciences, Beijing 100190, People's Republic of China*

Fanfan Wu − *Beijing National Laboratory for Condensed Matter Physics and Institute of Physics, Chinese Academy of Sciences, Beijing 100190, People's Republic of China; School of Physical Sciences, University of Chinese Academy of Sciences, Beijing 100190, People's Republic of China*

Luojun Du − *Beijing National Laboratory for Condensed Matter Physics and Institute of Physics, Chinese Academy of Sciences, Beijing 100190, People's Republic of China; School of Physical Sciences, University of Chinese Academy of Sciences, Beijing 100190, People's Republic of China*

Kenji Watanabe − *Research Center for Electronic and Optical Materials, National Institute for Materials Science, Tsukuba 305-0044, Japan*; orcid.org/0000-0003-3701-8119

Takashi Taniguchi − *Research Center for Materials Nanoarchitectonics, National Institute for Materials Science, Tsukuba 305-0044, Japan*; orcid.org/0000-0002-1467-3105

Dongxia Shi − *Beijing National Laboratory for Condensed Matter Physics and Institute of Physics, Chinese Academy of*

https://doi.org/10.1021/acs.nanolett.4c01411
Nano Lett. 2024, 24, 6722−6729

Sciences, Beijing 100190, People's Republic of China; School of Physical Sciences, University of Chinese Academy of Sciences, Beijing 100190, People's Republic of China; Songshan Lake Materials Laboratory, Dongguan 523808, People's Republic of China

Complete contact information is available at: https://pubs.acs.org/10.1021/acs.nanolett.4c01411

Author Contributions

W.Y. and G.Z. supervised the project. W.Y. and L.L. designed the experiments. Y.Y. and L.L. fabricated the devices. Y.Y. and L.L. performed the magneto-transport measurements. L.L. performed the calculations. K.W. and T.T. provided hexagonal boron nitride crystals. Y.Y., L.L., G.Z., and W.Y. analyzed the data. Y.Y., L.L., G.Z., and W.Y. wrote the paper with the input from all the authors.

Author Contributions

[#]Y.Y. and L.L. contributed equally to this work.

Notes

The authors declare no competing financial interest.

■ ACKNOWLEDGMENTS

We acknowledge support from the National Key Research and Development Program (Grant Nos. 2020YFA0309600, 2021YFA1202900), National Natural Science Foundation of China (NSFC, Grant Nos. 12074413, 61888102), the Strategic Priority Research Program of CAS (Grant No. XDB33000000), and the Key-Area Research and Development Program of Guangdong Province (Grant No. 2020B0101340001). K.W. and T.T. acknowledge support from the JSPS KAKENHI (Grant Nos. 20H00354, 21H05233, 23H02052) and World Premier International Research Center Initiative (WPI), MEXT, Japan.

■ REFERENCES

(1) Eisenstein, J. P.; Boebinger, G. S.; Pfeiffer, L. N.; West, K. W.; He, S. New fractional quantum Hall state in double-layer two-dimensional electron systems. *Phys. Rev. Lett.* **1992**, *68*, 1383−1386.
(2) Suen, Y. W.; Engel, L. W.; Santos, M. B.; Shayegan, M.; Tsui, D. C. Observation of a ν=1/2 fractional quantum Hall state in a double-layer electron system. *Phys. Rev. Lett.* **1992**, *68*, 1379−1382.
(3) Eisenstein, J. P.; MacDonald, A. H. Bose−Einstein condensation of excitons in bilayer electron systems. *Nature* **2004**, *432*, 691−694.
(4) Fogler, M. M.; Butov, L. V.; Novoselov, K. S. High-temperature superfluidity with indirect excitons in van der Waals heterostructures. *Nat. Commun.* **2014**, *5*, 4555.
(5) Du, L.; et al. Evidence for a topological excitonic insulator in InAs/GaSb bilayers. *Nat. Commun.* **2017**, *8*, 1971.
(6) Li, J. I. A.; Taniguchi, T.; Watanabe, K.; Hone, J.; Dean, C. R. Excitonic superfluid phase in double bilayer graphene. *Nat. Phys.* **2017**, *13*, 751−755.
(7) Liu, X.; Watanabe, K.; Taniguchi, T.; Halperin, B. I.; Kim, P. Quantum Hall drag of exciton condensate in graphene. *Nat. Phys.* **2017**, *13*, 746−750.
(8) Ma, L.; et al. Strongly correlated excitonic insulator in atomic double layers. *Nature* **2021**, *598*, 585−589.
(9) Liu, X.; et al. Crossover between strongly coupled and weakly coupled exciton superfluids. *Science* **2022**, *375*, 205−209.
(10) Cao, Y.; et al. Correlated insulator behaviour at half-filling in magic-angle graphene superlattices. *Nature* **2018**, *556*, 80−84.
(11) Cao, Y.; et al. Unconventional superconductivity in magic-angle graphene superlattices. *Nature* **2018**, *556*, 43−50.
(12) Cao, Y.; et al. Tunable correlated states and spin-polarized phases in twisted bilayer-bilayer graphene. *Nature* **2020**, *583*, 215−220.
(13) Liu, X.; et al. Tunable spin-polarized correlated states in twisted double bilayer graphene. *Nature* **2020**, *583*, 221−225.
(14) Shen, C.; et al. Correlated states in twisted double bilayer graphene. *Nat. Phys.* **2020**, *16*, 520−525.
(15) Serlin, M.; et al. Intrinsic quantized anomalous Hall effect in a moiré heterostructure. *Science* **2020**, *367*, 900−903.
(16) Xu, S.; et al. Tunable van Hove singularities and correlated states in twisted monolayer-bilayer graphene. *Nat. Phys.* **2021**, *17*, 619−626.
(17) Park, J. M.; Cao, Y.; Watanabe, K.; Taniguchi, T.; Jarillo-Herrero, P. Tunable strongly coupled superconductivity in magic-angle twisted trilayer graphene. *Nature* **2021**, *590*, 249−255.
(18) Zhang, Y.; et al. Promotion of superconductivity in magic-angle graphene multilayers. *Science* **2022**, *377*, 1538−1543.
(19) Bistritzer, R.; MacDonald, A. H. Moiré bands in twisted double-layer graphene. *Proc. Natl. Acad. Sci. U. S. A.* **2011**, *108*, 12233−12237.
(20) Po, H. C.; Zou, L.; Vishwanath, A.; Senthil, T. Origin of Mott Insulating Behavior and Superconductivity in Twisted Bilayer Graphene. *Phys. Rev. X* **2018**, *8*, 031089.
(21) Tarnopolsky, G.; Kruchkov, A. J.; Vishwanath, A. Origin of Magic Angles in Twisted Bilayer Graphene. *Phys. Rev. Lett.* **2019**, *122*, 106405.
(22) Lee, J. Y.; et al. Theory of correlated insulating behaviour and spin-triplet superconductivity in twisted double bilayer graphene. *Nat. Commun.* **2019**, *10*, 5333.
(23) Lisi, S.; et al. Observation of flat bands in twisted bilayer graphene. *Nat. Phys.* **2021**, *17*, 189−193.
(24) de Vries, F. K.; et al. Combined Minivalley and Layer Control in Twisted Double Bilayer Graphene. *Phys. Rev. Lett.* **2020**, *125*, 176801.
(25) Phinney, I. Y.; et al. Strong Interminivalley Scattering in Twisted Bilayer Graphene Revealed by High-Temperature Magneto-Oscillations. *Phys. Rev. Lett.* **2021**, *127*, 056802.
(26) Rickhaus, P.; et al. Correlated electron-hole state in twisted double-bilayer graphene. *Science* **2021**, *373*, 1257−1260.
(27) Tomić, P.; et al. Scattering between Minivalleys in Twisted Double Bilayer Graphene. *Phys. Rev. Lett.* **2022**, *128*, 057702.
(28) Kim, Y.; Moon, P.; Watanabe, K.; Taniguchi, T.; Smet, J. H. Odd Integer Quantum Hall States with Interlayer Coherence in Twisted Bilayer Graphene. *Nano Lett.* **2021**, *21*, 4249−4254.
(29) He, M.; et al. Symmetry breaking in twisted double bilayer graphene. *Nat. Phys.* **2021**, *17*, 26−30.
(30) Liu, L.; et al. Isospin competitions and valley polarized correlated insulators in twisted double bilayer graphene. *Nat. Commun.* **2022**, *13*, 3292.
(31) Liu, L.; et al. Observation of First-Order Quantum Phase Transitions and Ferromagnetism in Twisted Double Bilayer Graphene. *Phys. Rev. X* **2023**, *13*, 031015.
(32) Liu, L.; et al. Quantum oscillations in field-induced correlated insulators of a moiré superlattice. *Sci. Bull.* **2023**, *68*, 1127−1133.
(33) Kim, K.; et al. van der Waals Heterostructures with High Accuracy Rotational Alignment. *Nano Lett.* **2016**, *16*, 1989−1995.
(34) Pizzocchero, F.; et al. The hot pick-up technique for batch assembly of van der Waals heterostructures. *Nat. Commun.* **2016**, *7*, 11894.
(35) Purdie, D. G.; et al. Cleaning interfaces in layered materials heterostructures. *Nat. Commun.* **2018**, *9*, 5387.
(36) Zou, K.; Hong, X.; Zhu, J. Effective mass of electrons and holes in bilayer graphene: Electron-hole asymmetry and electron-electron interaction. *Phys. Rev. B* **2011**, *84*, 085408.
(37) Lee, K.; Jung, J.; Fallahazad, B.; Tutuc, E. Transport spectroscopy in bilayer graphene using double layer heterostructures. *2D Mater.* **2017**, *4*, 035018.
(38) Sanchez-Yamagishi, J. D.; et al. Quantum Hall Effect, Screening, and Layer-Polarized Insulating States in Twisted Bilayer Graphene. *Phys. Rev. Lett.* **2012**, *108*, 076601.

(39) Cheng, B.; et al. Gate-Tunable Landau Level Filling and Spectroscopy in Coupled Massive and Massless Electron Systems. *Phys. Rev. Lett.* **2016**, *117*, 026601.
(40) Mreńca-Kolasińska, A.; et al. Quantum capacitive coupling between large-angle twisted graphene layers. *2D Mater.* **2022**, *9*, 025013.
(41) Fang, J.; Vandenberghe, W. G.; Fischetti, M. V. Microscopic dielectric permittivities of graphene nanoribbons and graphene. *Phys. Rev. B* **2016**, *94*, 045318.
(42) Rickhaus, P.; et al. The electronic thickness of graphene. *Sci. Adv.* **2020**, *6*, No. eaay8409.
(43) Bykov, A. A. Nonlinear magnetotransport in a high-mobility quasi-two-dimensional electron system. *JETP Lett.* **2008**, *88*, 64−68.
(44) Mamani, N. C.; et al. Classical and quantum magnetoresistance in a two-subband electron system. *Phys. Rev. B* **2009**, *80*, 085304.
(45) Wiedmann, S.; Gusev, G. M.; Raichev, O. E.; Bakarov, A. K.; Portal, J. C. Thermally activated intersubband scattering and oscillating magnetoresistance in quantum wells. *Phys. Rev. B* **2010**, *82*, 165333.
(46) Dmitriev, I. A.; Mirlin, A. D.; Polyakov, D. G.; Zudov, M. A. Nonequilibrium phenomena in high Landau levels. *Rev. Mod. Phys.* **2012**, *84*, 1709−1763.
(47) Bykov, A. A.; et al. Beats of Quantum Oscillations of the Resistance in Two-Subband Electron Systems in Tilted Magnetic Fields. *JETP Lett.* **2019**, *109*, 400−405.
(48) Minkov, G. M.; et al. Magneto-intersubband oscillations in two-dimensional systems with an energy spectrum split due to spin-orbit interaction. *Phys. Rev. B* **2020**, *101*, 245303.
(49) Leeb, V.; Knolle, J. Theory of difference-frequency quantum oscillations. *Phys. Rev. B* **2023**, *108*, 054202.
(50) Raikh, M. E.; Shahbazyan, T. V. Magnetointersubband oscillations of conductivity in a two-dimensional electronic system. *Phys. Rev. B* **1994**, *49*, 5531−5540.
(51) Mamani, N. C.; Gusev, G. M.; Raichev, O. E.; Lamas, T. E.; Bakarov, A. K. Nonlinear transport and oscillating magnetoresistance in double quantum wells. *Phys. Rev. B* **2009**, *80*, 075308.
(52) Li, X.; Wu, F.; Das Sarma, S. Phonon scattering induced carrier resistivity in twisted double-bilayer graphene. *Phys. Rev. B* **2020**, *101*, 245436.
(53) Chu, Y.; et al. Temperature-linear resistivity in twisted double bilayer graphene. *Phys. Rev. B* **2022**, *106*, 035107.
(54) Li, H.; et al. Rapid and Reliable Thickness Identification of Two-Dimensional Nanosheets Using Optical Microscopy. *ACS Nano* **2013**, *7*, 10344−10353.
(55) Graf, D.; et al. Spatially Resolved Raman Spectroscopy of Single- and Few-Layer Graphene. *Nano Lett.* **2007**, *7*, 238−242.
(56) Koshino, M. Band structure and topological properties of twisted double bilayer graphene. *Phys. Rev. B* **2019**, *99*, 235406.

https://doi.org/10.1021/acs.nanolett.4c01411
Nano Lett. 2024, 24, 6722−6729